CHEMISTRY OF MATERIALS
Cite This: Chem. Mater. 2020, 32, 498−509
Article
pubs.acs.org/cm

High Loading Capacity Nanoencapsulation and Release of Hydrophobic Drug Nanocrystals from Microgel Particles

Trystan Domenech and Patrick S. Doyle*

Department of Chemical Engineering, Massachusetts Institute of Technology, Cambridge, Massachusetts 02139, United States

Supporting Information

ABSTRACT: Nanosizing of active pharmaceutical ingredients (APIs) is a key approach to improve their bioavailability, particularly in the case of water-insoluble compounds. Moreover, enabling the high load encapsulation of stable API nanocrystals is desirable for their tunable dosing in final products, as well as for further pharmaceutical formulation steps where the active compounds are often diluted with excipients or other additives. Yet, these remain challenging goals due to the lack of a simple and scalable approach. Using nanoemulsion templating in microgel particles, we demonstrate that stable API nanocrystal-loaded particles can be easily synthesized up to high drug loads (>70%) via a scalable, low-energy process. Our study shows that the drug release kinetics has a nonlinear dependence on the drug load of the microgel particles, where internal packing of the nanocrystals influences their release from the microgel matrix as the drug load increases. Despite the wide range of dissolution time scales, all of the dissolution profiles can be rescaled using only two adjustable parameters. The effect of particle size can also be used to tune the release rate, and significant dissolution enhancement is observed (up to 70×) compared to bulk API crystals, including at the highest drug load.

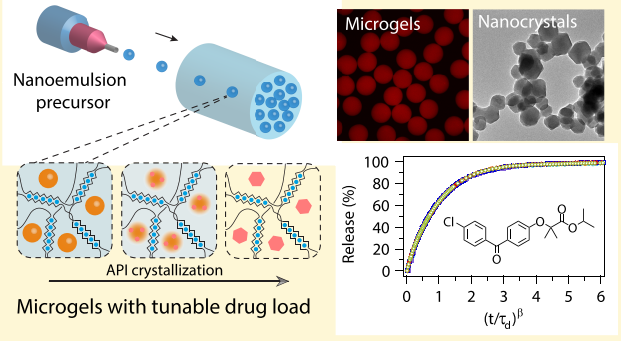

Bioavailability, the propensity of a compound to reach the circulatory system, is an essential factor in drug metabolism and, therefore, of paramount importance in the design of pharmaceutical drugs. According to the Biopharmaceutical Classification System (BCS), the bioavailability of drugs is limited by either their solubility or their intestinal permeability.[1,2] The majority of drugs in development are poorly soluble in water due to their hydrophobic nature,[3] which negatively impacts their bioavailability. This is particularly detrimental to drug delivery performance in the case of oral administration, where poor drug dissolution in the gastrointestinal tract leads to low absorption levels. Therefore, significant emphasis is placed on ways of improving the solubility of hydrophobic drugs to leverage bioavailability issues and ensure successful new drug development.[4]

In this regard, the comminution of active pharmaceutical ingredient (API) crystals below the micron scale, or nanosizing, is an efficient approach to improve the dissolution properties of hydrophobic drugs due to the higher surface area/volume ratio of nanocrystals comparatively to bulk API crystals.[5,6] The nanosizing of APIs is accomplished through either top-down[7] or bottom-up[8,9] routes, where bulk crystals are broken down into submicron crystals in the case of the former and controlled nanocrystal growth to the targeted size is carried out in the latter case. Technologies based on the combination of these two approaches were also developed in the pharmaceutical industry.[7] Among the existing nanosizing technologies, top-down strategies include[5,7] wet ball-milling and high-pressure homogenization, while bottom-up approaches comprise antisolvent precipitation,[8] high-gravity controlled precipitation,[10] spray drying,[11] and electrospraying.[12] These techniques, however, suffer from practical drawbacks, such as high energy costs, additives requirements,[8] limited production rates,[7] and poor polymorphism control.[13] Furthermore, the incorporation of stable hydrophobic nanocrystals into drug delivery medium, like porous matrixes, through these approaches leads to limited drug loads,[7,14−17] which undermines their efficiency for the engineering of oral drug delivery products. Indeed, high drug loads are desirable for dilution with excipients or other drugs during pharmaceutical formulation, as well as for efficient drug dosage or when minimizing the amount of certain excipients becomes critical due to their potentially negative impact on patients.[7]

In the present work, we demonstrate that high drug load nanoencapsulation of a nearly water-insoluble API inside microgel particles can be achieved through a scalable bottom-up approach based on low-energy nanoemulsification. Unlike microemulsions, nanoemulsions are thermodynamically unstable, yet kinetically stable, emulsions (i.e., dispersions of a liquid phase into another, where both liquids are immiscible) with a typical droplet size <500 nm.[18−20] Nanoemulsions have found many industrially relevant applications, including drug delivery,[21,22] food engineering,[23,24] or topical cosmetic

Received: October 16, 2019
Revised: December 12, 2019
Published: December 13, 2019

DOI: 10.1021/acs.chemmater.9b04241
Chem. Mater. 2020, 32, 498−509

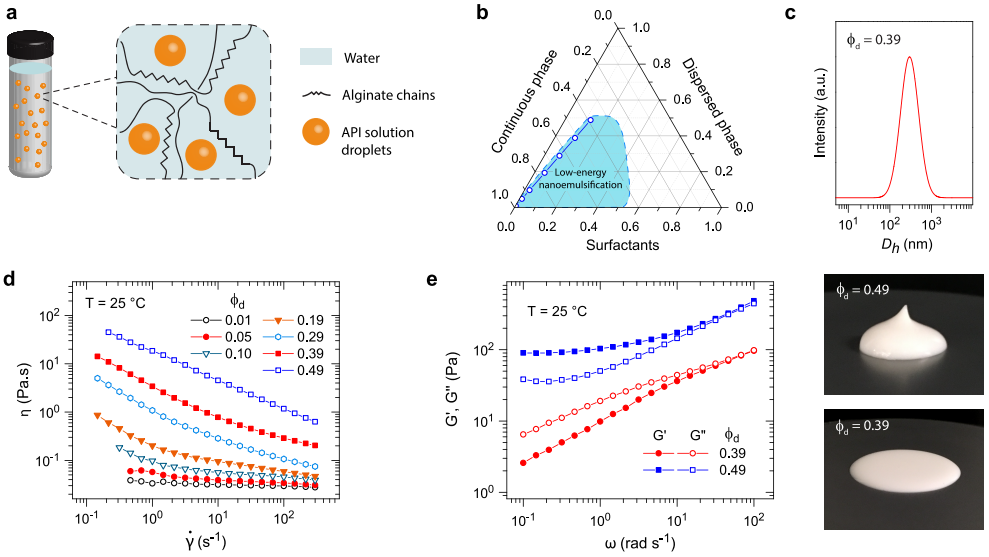

Figure 1. Nanoemulsion formation and viscoelastic properties. (a) Kinetically stable nanoemulsions are generated via a low-energy spontaneous nanoemulsification route using a blend of anionic surfactants Span 80 and Tween 80 (HLB = 13.5), where a fenofibrate-in-anisole solution is progressively dispersed into the continuous phase. The latter is a sodium alginate-in-water solution, a precursor to the microgel particles. (b) Ternary composition diagram showing the region of low-energy nanoemulsification employed here (each axis is expressed in volume fraction). Blue circles show the chosen compositions, with a fixed SOR = 0.25 and a dispersed phase volume fraction ϕ_d spanning from 0.01 to 0.49. (c) DLS measurement of the droplet size (hydrodynamic diameter, D_h) distribution for ϕ_d = 0.39. (d) Viscosity−shear rate flow curves at 25 °C for the nanoemulsions at the indicated ϕ_d from 0.01 to 0.49. (e) Linear viscoelastic spectra of the nanoemulsions for ϕ_d = 0.39 (red circles) and ϕ_d = 0.49 (blue squares). G', filled symbols; G'', empty symbols. The transition from a viscous liquid at ϕ_d = 0.39 to a pastelike texture at ϕ_d = 0.49 is readily apparent from the digital pictures (right panel).

formulations,[25] and can be formed by high- or low-energy methods.[20] Here, cross-linkable oil-in-water nanoemulsions were prepared using alginate as an ionotropic gelator in the continuous aqueous phase. Fenofibrate, a highly hydrophobic drug (log P = 5.24)[26] typically delivered orally to treat high blood lipoprotein concentrations, was used as a model drug. This water-insoluble compound (<1 μg mL^{-1}) was solvated in anisole, an aromatic ether used as the "oil" phase, and finely dispersed into the continuous aqueous phase. The obtained nanoemulsions were then used as precursors for the centrifugal synthesis of microgel particles. These materials possess two distinctive length scales, the microgel particle size and the nanoemulsion droplet size, where the nanoemulsion droplet size is typically ∼3 orders of magnitude smaller than the microgel particle it is contained in. Drug nanocrystallization was carried out in a subsequent evaporation step. The principle of this crystallization approach is as follows: the surfactant-stabilized nanoemulsion droplets are isolated from each other within the cross-linked hydrogel network, which prevents the droplets from ripening and coalescence; then, precipitation of the drug occurs in the confinement of the nanoemulsion droplet during evaporation and cannot grow further than the droplet boundary.[27] Thereby, the microgel particles become a porous solid loaded with drug nanocrystals after completion of the drying step. Combining X-ray diffraction (XRD), calorimetry, and electron microscopy, the characterization of the drug-nanocrystal-loaded microgel particles was then performed and used to interpret the drug release properties of these systems. Our results reveal that low-energy nanoemulsification can successfully lead to high drug load microgel particles by optimization of the surfactant amount. Even though the release profiles of these microgel particles follow a rather simple scaling law, the release kinetics depends on the drug load, which we link to an internal change of particle structure due to the nanocrystal distribution. We also demonstrate that these materials can be engineered to obtain a fast release of an active hydrophobic compound, comparable to the state-of-the-art commercial formulation, while reaching high drug loads, which is unprecedented to our knowledge.

RESULTS AND DISCUSSION

Cross-Linkable Nanoemulsion Synthesis and Viscoelasticity. The dispersed organic oil phase (a fenofibrate solution in anisole) was emulsified in the continuous aqueous phase (an alginate solution) and kinetically stabilized using a blend of nonionic surfactants (sorbitan monooleate Span 80 and polysorbate Tween 80). First, the surfactants were dispersed in the continuous phase under rigorous magnetic stirring. The dispersed phase was then progressively pipetted dropwise into the continuous phase while maintaining stirring until a given dispersed phase volume fraction ϕ_d was reached, and emulsification was left to proceed for 10 min at room temperature (∼23 °C). This low-energy procedure led to kinetically stable oil-in-water nanoemulsions (Figure 1a) through a phenomenon known as spontaneous emulsification,[28−30] where a fine dispersion of droplets is formed under minimal mixing energy input. Although there is currently no definitive mechanistic consensus about the process of spontaneous emulsification, it is often hypothesized that nanoemulsification results from the formation and breakup of a bicontinuous microemulsion at the boundary region between the oil and water phase.[31,32] The resulting size distribution of the droplets is sensitive to composition parameters, such as the type and amount of the organic solvent and surfactants, and to mixing procedures.[32−34] One important factor for the droplet size and kinetic stability of nanoemulsions is the hydrophilic−

DOI: 10.1021/acs.chemmater.9b04241
Chem. Mater. 2020, 32, 498−509

lipophilic balance (HLB), which dictates the partitioning of a given surfactant into both oil and water phases,[32,35,36] i.e., the higher the HLB, the more the surfactant partitions into the water phase rather than into the oil phase and vice versa. Our nanoemulsions were produced using a Span 80/Tween 80 blend (14/86 wt %) with a HLB of 13.5 (the HLBs of Span 80 and Tween 80 are 4.3 and 15, respectively), which was selected for the strong time-stability of the droplet sizes. Unlike high-energy methods, where the oil phase is broken down into submicron droplets through intense shear stresses and can be stabilized by a relatively low amount of surfactants,[37] low-energy spontaneous emulsification usually requires a higher surfactant/oil ratio[38] (SOR). Figure 1b illustrates the approximate mapping for the region of low-energy spontaneous nanoemulsification on the ternary composition diagram, where both the amounts of surfactants and dispersed phase reach an upper limit due to the high viscosities, which makes it difficult to carry out homogeneous mixing. Based on this practical limitation, we prepared nanoemulsions up to a droplet volume fraction $\phi_d \approx 0.5$. It is noteworthy that, in the case of pure water as the continuous phase (less viscous than the alginate solution used here), the formation of concentrated nanoemulsions up to $\phi_d \approx 0.65$ is reported in the literature, with phase inversion occurring at higher oil phase volume fractions.[37,39] Given that the drug load of the microgel particles decreases as the amount of surfactants used to prepare the nanoemulsions increases, we sought to determine the minimal amount of surfactants necessary to obtain well-defined nanoemulsions using this low-energy approach. Usually, this minimal amount corresponds to a SOR of ∼0.5−1,[32,38,40] although it is system-specific. Here, we found that nanoemulsions can be produced with a SOR as low as 0.25. The symbols in Figure 1b correspond to the selected nanoemulsion compositions, where ϕ_d was varied from 0.01 up to 0.49 with a fixed SOR of 0.25. As shown by dynamic light scattering (DLS) measurements, the obtained nanoemulsions have a monomodal size distribution, with an average hydrodynamic diameter $\bar{D}_h = 291 \pm 6$ nm and a polydispersity index (PDI) = 0.30 ± 0.02 for $\phi_d = 0.39$ (Figure 1c). The droplet size distribution was not found to significantly depend on ϕ_d (see Supporting Information Figure S2a).

As colloidal systems, nanoemulsions can display a wide variety of flow properties where droplet size and volume fraction have a significant impact on their viscoelasticity.[18,20,41] The rheology of our cross-linkable nanoemulsions is central in regards to their processing into microgel particles, where they have to flow through a capillary (needle tip) to form drops and allow for bulk diffusion of cations to induce cross-linking of the alginate chains in the continuous phase. The steady-state flow curves of the nanoemulsions are shown in Figure 1d, which clearly mark the non-Newtonian nature of these materials, i.e., the viscosity η is not independent of the shear rate $\dot{\gamma}$. More specifically, we observe a shear-thinning behavior (i.e., a decrease of η when $\dot{\gamma}$ increases) that is increasingly pronounced as ϕ_d increases. Furthermore, the viscosity of the nanoemulsions increases with the droplet concentration at all shear rate values. The relative viscosity η_r (defined as the nanoemulsion/continuous phase viscosity ratio) as a function of ϕ_d at high shear rates was well described by the Quemada model,[42] $\eta_r = (1 - \phi_d/\phi_M)^{-2}$, where the maximum packing fraction ϕ_M was used as the only fitting parameter and found to be ∼0.62 (see Supporting Information Figure S2b), i.e., close to the value for the random close packing of monodisperse spheres,[43] $\phi_{rcp} \approx 0.64$, and consistent with rheological data of other nanoemulsions from the literature.[44] The nanoemulsion viscosity approximately ranges from 0.03 to 0.7 Pa s at higher shear rates, which is low enough for them to be extruded through the capillary used for particle synthesis. However, we observed a qualitative shift in the texture of the nanoemulsions at higher droplet concentrations, where a liquid texture was observed for ϕ_d up to 0.39, while a self-standing paste was obtained at $\phi_d = 0.49$ (see pictures in Figure 1e). This liquid-to-paste transition was confirmed by linear viscoelastic measurements, where a viscoelastic liquidlike relaxation, i.e., both elastic (G') and viscous (G'') moduli decrease with the angular frequency (ω) and $G'' > G'$, was observed at $\phi_d = 0.39$, while a solidlike behavior, marked by $G' > G''$ and a G' plateau at lower angular frequencies, was found in the case of $\phi_d = 0.49$ (Figure 1e). Such a solidlike viscoelastic response has been observed before in concentrated nanoemulsions,[18,41,45,46] where the transition point depends on the droplet size. In our case, this solidlike dynamics means that the fast diffusion of cations in the continuous phase of the cross-linkable nanoemulsions, which is necessary to form cross-links between the alginate chains and form a volume-spanning elastic network during the microgel particle synthesis process, will be hindered. Therefore, microgel particles were synthesized using nanoemulsions with ϕ_d up to 0.39 as precursors.

Microgel Particle Synthesis and Nanocrystal Formation. Multiple types of microparticle designs for drug delivery applications have been developed in the past decade,[47,48] where the microstructure of the particles can be engineered to achieve the desired release properties. From a practical standpoint, these materials, often based on polymer gels, are attractive due to the commercial availability of their precursors, as well as due to the relative ease of their production methods. Here, our cross-linkable nanoemulsions were transformed into microgel particles by centrifugal synthesis,[49] where the liquid material was placed into a syringe and pushed through a capillary (a needle tip) using the centrifugal force to form drops from filament breakup based on the Plateau−Rayleigh instability, followed by cross-linking of the alginate solution in the continuous phase of the drops by harvesting them in an aqueous calcium chloride solution (575 mM) reservoir (Figure 2a). The concentration in Ca^{2+} cations in the collecting reservoir was high enough for the ionotropic complexation to occur almost instantaneously at the drop surface as it entered the reservoir, and the particles were kept into the Ca^{2+} solution for 1 h to complete the cross-linking reaction via the cation diffusion toward the center of the particles. The particles were then collected by filtration and washed in deionized (DI) water. Additionally, particle synthesis was repeated using nanoemulsion precursors, where Nile red, a lipophilic fluorescent dye, was co-encapsulated along with fenofibrate in the anisole solution to visualize the homogeneity of the nanoemulsion droplet distribution within the particles, which did not impact the nanoemulsion droplet size. We obtained uniform microgel particles with monodisperse size distribution (Figure 2b), with an average diameter of 351 μm [coefficient of variation (CV) = 3.7%, roundness = 0.95]. This particle size is in good agreement with theoretical prediction,[49] assuming that cross-linking has a negligible impact on the particle size (i.e., the cross-linked particle size is approximately the same as the drop size before it enters the Ca^{2+} bath), which states that $(d_p/d_0)^3 = 0.9372\mathrm{Bo}^{-1.07}$, with the Bond number $\mathrm{Bo} = \rho G d_0/4\gamma$ expressing the ratio between

DOI: 10.1021/acs.chemmater.9b04241
Chem. Mater. 2020, 32, 498−509

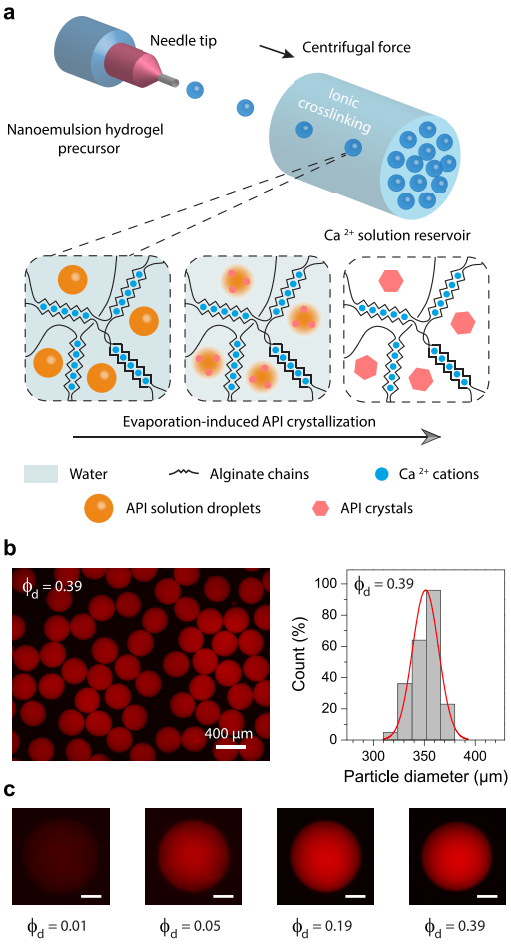

Figure 2. Synthesis of nanoemulsion-loaded microgel particles. (a) Scheme of the centrifugal synthesis process and subsequent evaporation-induced drug nanocrystallization. Nanoemulsion drops are generated using the centrifugal force through a needle tip and collected into a calcium chloride bath, where the G blocks of the alginate chains rapidly form ionic cross-links via Ca^{2+} cations, leading to the ionotropic gelation of the continuous phase of the nanoemulsion. Both water and anisole phases are then evaporated out of the microgel particles to precipitate the fenofibrate into nanocrystals within the alginate matrix. (b) Fluorescence microscopy image and size distribution of wet microgel particles with $\phi_d = 0.39$ nanoemulsion. The observed fluorescence intensity comes from the Nile red dye co-encapsulated with the fenofibrate inside the nanoemulsion droplets. Average particle diameter = 351 μm, CV = 3.7% (c) Particle-scale fluorescence microscopy images of wet microgel particles containing nanoemulsions with ϕ_d ranging from 0.01 to 0.39. Scale bars correspond to 100 μm.

centrifugal forces and surface tension, where d_p is the particle diameter, d_0 is the internal diameter of the needle tip, ρ is the liquid density, G is the centrifugal acceleration, and γ is the liquid surface tension. Using $d_0 = 150$ μm, $\rho = 1$ g cm^{-3}, $G = 1078$ m s^{-2}, and $\gamma = 0.072$ N m^{-1}, this gives $d_p \approx 355$ μm. As shown in Figure 2c, the droplet distribution inside the microgel particles appears homogeneous across the ϕ_d range. This centrifugal synthesis setup enables particle production at a throughput of ~20 mL h^{-1}, i.e., ~88 × 10^4 particles h^{-1} for this particle size.

Crystallization of the fenofibrate encapsulated in the nanoemulsion droplets within the microgel particles was performed by evaporation of both liquid phases (water and anisole). This drying step was carried out by placing the particles in an oven at 50 °C for 4 days. As a result of evaporation, the particles shrank during the drying process, which was characterized by the shrinking ratio $S_r = d_{dry}/d_p$, where d_{dry} is the dried particle final diameter. The extent of shrinking depends on the particle elasticity and therefore on the alginate concentration in the continuous phase. Here, we find $S_r = 0.68 \pm 0.03$, corresponding to $d_{dry} = 239 \pm 9$ μm. The dependence of dried particle drug load on the dispersed phase volume fraction ϕ_d of the nanoemulsion precursors is presented in Figure 3. It is noticeable that high drug loads

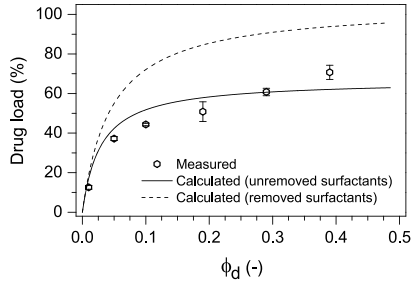

Figure 3. Drug load of the dried microgel particles as a function of the volume fraction of the dispersed phase (ϕ_d) of the nanoemulsion precursor. Data represent mean ± standard deviation. The solid line corresponds to eq 1 with $\varsigma = 0.25$ (complete surfactant retention in the particles); the dashed line corresponds to eq 1 with $\varsigma = 0$ (complete surfactant removal from the particles).

were typically obtained for $\phi_d > 0.1$, with a very high value (>70%) reached for $\phi_d = 0.39$. The theoretical drug load of the dried microgel particles can be calculated as follows

$$\Lambda = \frac{x_{api}}{x_{api} + \varsigma + \frac{x_c}{x_d} x_{alg}} \quad (1)$$

where Λ is the drug load, ς is the SOR, x_{api} is the mass fraction of fenofibrate in the dispersed phase, x_{alg} is the mass fraction of alginate in the continuous phase, and x_c and x_d are the mass fractions of the continuous and dispersed phases relative to the total nanoemulsion mass, respectively. Here, both x_{api} and x_{alg} are constant (45 and 2 wt %, respectively), while x_c and x_d depend on the nanoemulsion formulation. The continuous curves in Figure 3 correspond to the theoretical drug load for two cases: one in the hypothesis of total retention of the surfactants in the particles (i.e., $\varsigma = 0.25$ in eq 1), and the other in the hypothesis of complete removal of the surfactants from the particles (i.e., $\varsigma = 0$ in eq 1). Even though surfactants do not evaporate during drying, there is indeed an uncertainty regarding the amount of excess surfactants that can be washed away during the particle rinsing steps prior to the drying procedure, and the two aforementioned hypotheses represent both extreme scenarios. Remarkably, the measured drug load values progressively get closer and eventually exceed the calculated values in the hypothesis of total surfactant retention as ϕ_d increases (Figure 3), which indicates that less surfactants remain in the dried particles when the nanoemulsion concentration increases. Given that the nanoemulsions are prepared at a fixed SOR, the excess surfactants (i.e., the surfactants that do not partition at the crowded oil−water interface) tend to accumulate in the microgel particles when ϕ_d increases. We therefore attribute this trend in drug load vs ϕ_d

DOI: 10.1021/acs.chemmater.9b04241
Chem. Mater. 2020, 32, 498−509

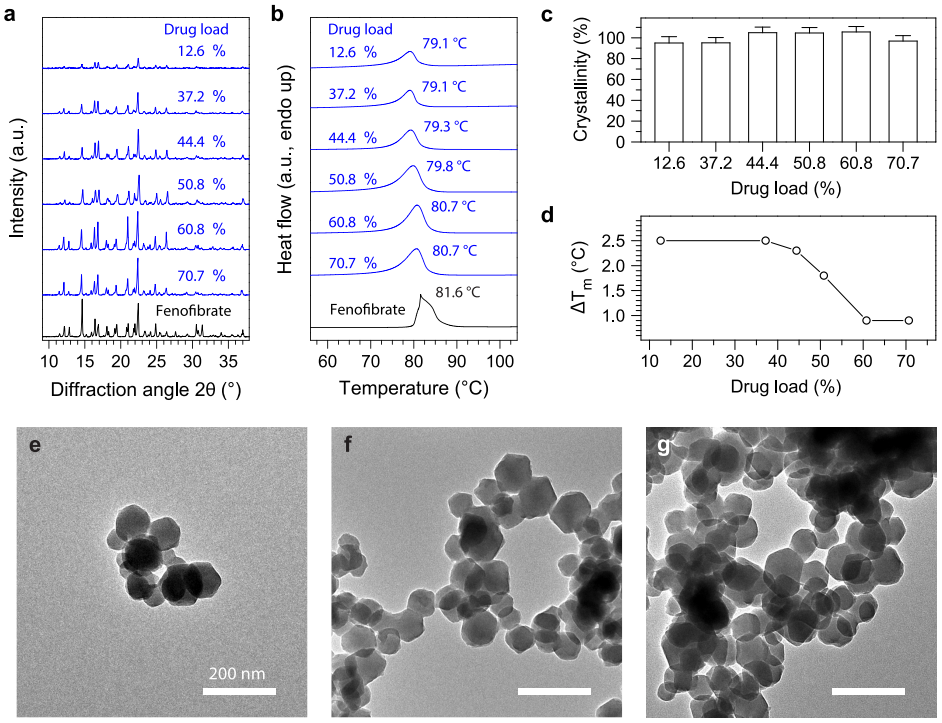

Figure 4. Physical characterization of the encapsulated fenofibrate nanocrystals. (a) X-ray diffractograms and (b) DSC thermograms comparing bulk fenofibrate to the fenofibrate nanocrystals loaded in the dried microgel particles with drug loads ranging from 12.6 to 70.7%. The melting temperature (T_m) is indicated next to each endothermic peak. (c) Degree of crystallinity and (d) melting point depression of the fenofibrate nanocrystals loaded in the dried microgel particles as a function of particle drug load. Data represent mean ± standard deviation. (e–g) Bright-field TEM images of the recovered fenofibrate nanocrystals from the dried microgel particles with drug loads of 12.6, 44.4, and 70.7%, respectively. Scale bars correspond to 200 nm.

to the increased removal of excess surfactants at higher ϕ_d values during particles washing, prior to their drying.

We now turn to the physical characterization of the fenofibrate nanocrystals within the dried microgel particles. The polymorphic nature of fenofibrate has been well described in the literature, where the stable form I and the metastable form II have often been reported,[50−52] along with the more recent form III polymorph.[53] The arrangement of the fenofibrate molecules into aliphatic and aromatic layers leads to the more stable crystalline structure form I.[51,53] The powder X-ray diffraction (XRD) patterns of the dried particles at different drug loads and of bulk fenofibrate crystals are compared in Figure 4a. Similar XRD patterns are observed, confirming the crystalline nature of the fenofibrate encapsulated inside the dried microgel particles. The intensity of the diffraction peaks logically increases with the drug load of the particles. The main peaks are found at the diffraction angles (2θ) 12.1, 12.8, 14.6, 16.4, 16.9, 18.1, 19.5, 21.0, 22.0, 22.4, 24.9, 30.5, and 31.3°, which are typical of form I diffraction pattern.[16,51,52] Differential scanning calorimetry (DSC) analysis further supports the presence of fenofibrate crystals inside the particles, where an endothermic peak, corresponding to a melting point, is observed for each drug load (Figure 4b). Since APIs have a higher stability in the crystalline rather than in the amorphous form,[54] it is relevant to evaluate the degree of crystallinity of the fenofibrate encapsulated in the microgel particles. To this end, we measured the specific enthalpy of fusion of particles $\Delta H_{particles}$ by integration of the specific heat capacity curves and deduced the specific enthalpy of fusion of the fenofibrate crystals inside the particles as $\Delta H_{crystals} = \Delta H_{particles}/\Lambda$. The crystallinity of the encapsulated fenofibrate was defined as $\Delta H_{crystals}/\Delta H_{bulk}$, where ΔH_{bulk} is the specific enthalpy of fusion of bulk fenofibrate crystals (see Supporting Information Table S1). As shown in Figure 4c, our encapsulation process led to complete crystallization of the fenofibrate within the particles over the entire range of investigated drug load. Another characteristic of the nanocrystal-loaded particles is that their thermograms show a lower melting point compared to that of bulk fenofibrate (Figure 4b). Such melting point depression is typical of nanocrystals,[55,56] which is tied to their higher surface-to-volume ratio and reduced cohesive energy at the surface comparatively to bulk crystals. The theoretical relationship between the melting point depression ΔT_m and the size of the nanocrystals is given by the Gibbs−Thomson equation,[56] which is expressed as follows in the case of spherical nanocrystals[16,57]

$$\Delta T_m = T_{m,bulk} - T_{m,cryst} = 4V_m T_{m,bulk}\frac{C_T}{d_{cryst}} \quad (2)$$

where $T_{m,bulk}$ is the melting peak temperature of bulk crystals, $T_{m,cryst}$ is the melting peak temperature of nanocrystals, V_m is the molar volume of the crystals, C_T is the Turnbull coefficient, and d_{cryst} is the nanocrystal diameter. Herein, the melting point depression is found to depend on the microgel particle drug load (Figure 4d). We observe three distinct regions: a plateau at $\Delta T_m \approx 2.5$ °C up to $\Lambda \approx 40\%$, followed by a decrease in ΔT_m and a final plateau at $\Delta T_m \approx 1$ °C for $\Lambda > 60\%$. According to eq 2, this change in ΔT_m suggests that the size of the fenofibrate nanocrystals inside the particles increases when the drug load increases >40%. However, transmission electron microscopy (TEM) imaging revealed that the fenofibrate

DOI: 10.1021/acs.chemmater.9b04241
Chem. Mater. 2020, 32, 498−509

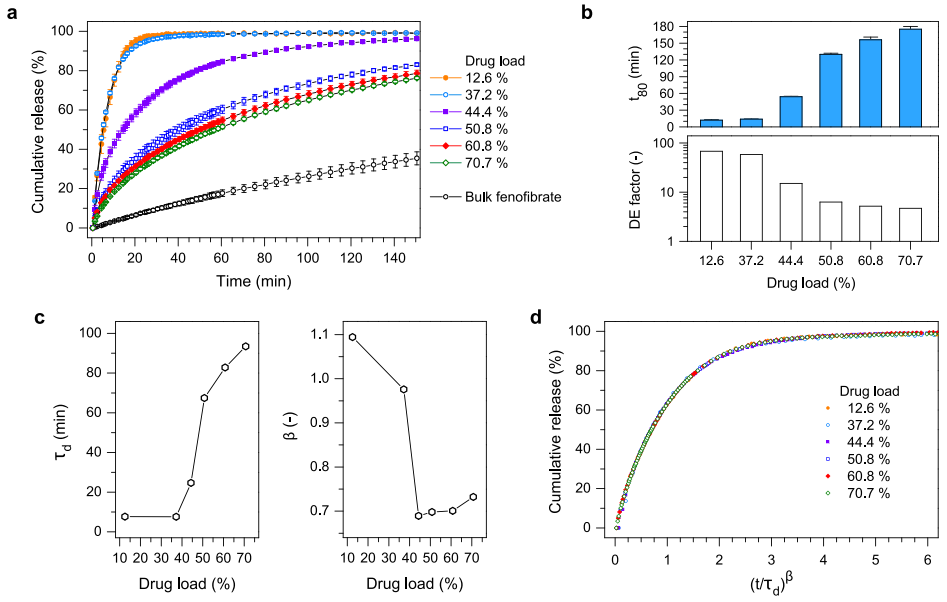

Figure 5. Influence of particle drug load on drug release kinetics. (a) Cumulative release profiles of bulk fenofibrate and 239 μm dried microgel particles with drug loads ranging from 12.6 to 70.7%. Data represent mean ± standard deviation. (b) Time at 80% drug release (top) and dissolution enhancement factor (bottom) as a function of particle drug load. (c) Fitting parameters of the Weibull equation, characteristic dissolution time τ_d (left), and shape parameter β (right), as a function of particle drug load. (d) Rescaled release profiles of the particles at various drug loads from the data represented in (a).

nanocrystals extracted from the microgel particles have similar size across the investigated drug load range (Figure 4e–g), where faceted nanocrystals with an average size of ∼115 nm were observed. The nanocrystal size depends on three parameters: the nanoemulsion droplet size, the API concentration in the nanoemulsion droplets, and the density of the precipitated solid nanoparticles. Assuming spherical nanocrystals, we can calculate it as follows

$$\frac{d_{cryst}}{d_{drop}} = \left(\frac{V_{cryst}}{V_{drop}}\right)^{1/3} = \left(\frac{C_{fen}}{\rho_{cryst}}\right)^{1/3} \quad (3)$$

where V_{cryst} is the nanocrystal volume, V_{drop} is the nanoemulsion droplet volume, $C_{fen} = m_{fen}/V_{drop}$ is the fenofibrate concentration in the nanoemulsion droplets, and ρ_{cryst} is the nanocrystal density. With C_{fen} = 0.48 g mL^{-1}, ρ_{cryst} = 1.2 g cm^{-3}, and assuming $d_{drop} \equiv \overline{D}_h \approx 291$ nm, eq 3 yields $d_{cryst} \approx$ 214 nm, a rather high value compared to the 115 nm found by TEM.

Such a discrepancy could arise from the nanocrystal extraction/alginate de-cross-linking procedure, which involves re-suspension of the nanocrystals in DI water and could potentially lead to their erosion by partial dissolution, even though the solubility of fenofibrate in pure water is extremely low (∼0.8 μg mL^{-1} at 25 °C[58]). Another reason could be the overestimation of the actual droplet size by DLS when assuming that the hydrodynamic diameter of the droplet is equivalent to the physical droplet size. In fact, similar overestimations of nanoemulsion droplet size by DLS comparatively to electron microscopy techniques have been reported in the literature.[59,60] Since the nanocrystal size does not depend upon the drug load of the microgel particles, we hypothesize that the change in melting point depression observed when Λ > 40% derives from the clustering of the hydrophobic API nanocrystals in the microgel particles during drying, as the nanocrystals get increasingly concentrated within the particles. To corroborate this premise, we calculated the internanocrystal separation distance within the dried microgel particles in the ideal case of evenly spaced nanocrystals (see the Supporting Information). We found that this separation becomes smaller than the nanocrystal size itself for Λ > 40%, which could foster the formation of heterogeneous nanocrystal clusters during the drying process due to the hydrophobic nature of fenofibrate. Several studies have demonstrated that the formation of larger structures based on nanocrystal assembly, including clusters, is associated with a decrease in ΔT_m compared to that of the primary nanocrystals.[61−64]

Influence of Microgel Particle Drug Load on Release Profiles. Drug release kinetics from the microgel particles was determined in vitro using a USPII standard dissolution device. Each series of particles were tested in identical sink conditions by adjusting the amount of particles based on their drug load (see Table S2). The release profiles of the microgel particles and bulk fenofibrate are regrouped in Figure 5a. It clearly appears that the nanocrystal-loaded microgel particles have a significantly faster release compared to bulk fenofibrate crystals, where the typical release time scale depends on the particle drug load. To quantify this, we plot the time at 80% release t_{80} and the dissolution enhancement (DE) factor, defined as $t_{80,bulk}/t_{80,particles}$ where $t_{80,bulk}$ = 815.5 min and $t_{80,particles}$, respectively, correspond to the time at 80% release for bulk fenofibrate and the microgel particles, as functions of the drug load in Figure 5b. A nonlinear dependence on the drug load is found, where $t_{80} \approx$ 12 min up to ∼40% in drug load and suddenly increases with the drug load. Correspondingly, a very high DE factor (∼70) is found up to ∼40% in drug load, which then decreases to ∼5 at the highest drug load. For the sake of benchmark comparison, the fast release observed with our particles up to ∼40% in drug load performs very well against other fenofibrate nanocrystal formulations obtained via alternative approaches, such as porous silica particles[16] ($t_{80} \approx$ 42.5 min, drug load ≈28%), tablets based on

DOI: 10.1021/acs.chemmater.9b04241
Chem. Mater. 2020, 32, 498−509

spray drying of nanosuspensions[15] ($t_{80} \approx 10$ min, drug load <10%), or commercially available TriCor tablets containing disintegrants ($t_{80} \approx 10$ min, drug load ≈23%), while having the advantage of higher drug loads.

The particle release profiles shown in Figure 5a were fitted using the Weibull cumulative distribution function

$$\frac{M_t}{M_\infty} = 1 - e^{\left(\frac{t}{\tau_d}\right)^\beta} \quad (4)$$

where M_t/M_∞ is the cumulative release, τ_d is the characteristic dissolution time [with $M_t(t = \tau_d)/M_\infty \sim 63.2\%$], and β is the shape parameter. An excellent agreement between the data and eq 4 was obtained regardless of the drug load (see Figure S7a). Unsurprisingly, the dependence of τ_d on the drug load follows the same trend as for t_{80}, while β decreases from values close to unity to ∼0.7 when the drug load >40% (Figure 5c). The entirety of the dissolution data across the whole range of particle drug load collapses nicely onto a master curve when plotted as a function of the dimensionless group $(t/\tau_d)^\beta$, as presented in Figure 5d. Even though the Weibull function has often been employed empirically to describe the release profiles of drugs from solid pharmaceutical dosage forms, the physical interpretation of the shape parameter β remains an open question.[65,66] Here, the sudden change in β seems to coincide with the slowdown of the dissolution kinetics observed for $\Lambda > 40\%$. As shown in Figure 6a, the increase in t_{80} at higher drug loads correlates with the decrease in melting point depression from DSC analysis (data from Figure 4d). This points to a slowdown in release kinetics caused by the effect of nanocrystal clustering at higher drug loads, where the mass transfer of the drug through the alginate matrix is impacted by the presence of clusters. To gain further insight into the dissolution behavior of the API from high-drug-load microgel particles, we conducted a dissolution experiment on particles with $\Lambda = 70.7\%$ where the dissolution was interrupted at $M_t/M_\infty \sim 50\%$ (corresponding to $t \sim 60$ min, see the green curve in Figure 5a); the remaining undissolved fraction of the particles was quickly recovered from the dissolution medium by filtration and dried into an oven at 50 °C. The recovered particles were analyzed using DSC. A comparison of the thermograms of the particles prior to and after 50% dissolution is presented in Figure 6b, where the melting peak temperature is nearly identical, indicating that the average nanocrystal size of the undissolved fraction is the same as the native particles. However, the melting peak appears much narrower after 50% dissolution, especially on the lower-temperature side, which indicates that most of the smaller population of the nanocrystal size distribution has been released from the particles before reaching 50% in cumulative release. In terms of release profile, the decrease of β from 1 to 0.7, typically observed at higher drug loads, translates into a higher slope (i.e., higher release rate) for $t < \tau_d$ (see Figure S8). Based on these observations, it is likely that the sudden drop in the shape parameter β at higher drug loads is reflective of the faster release of smaller nanocrystals from the microgel matrix compared to the slower release of nanocrystal clusters. This is further corroborated by the decrease of β when plotted as a function of τ_d (see Figure S10).

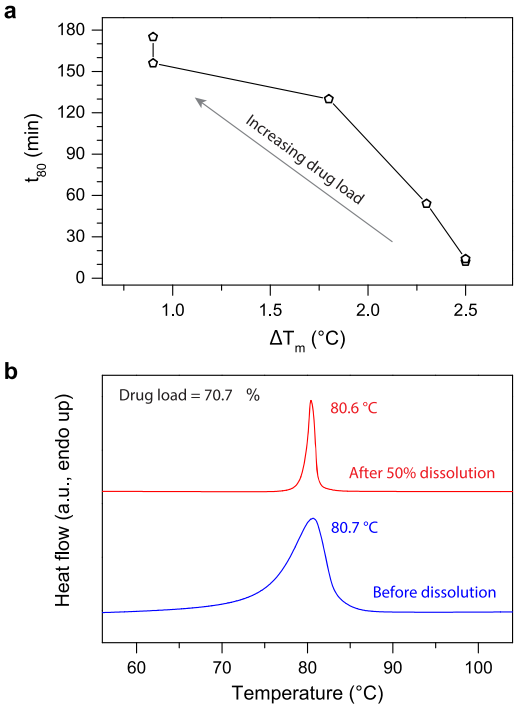

Figure 6. (a) Correlation between the time at 80% drug release and the melting point depression of the dried microgel particles at different drug loads. (b) DSC thermograms of 70.7% drug load dried microgel particles before dissolution (blue curve) and after 50% dissolution (red curve).

Despite the trend shown in Figure 5, the dissolution kinetics of high-drug-load particles can be modulated by adjusting the particle size. The release profiles for particles with $\Lambda = 70.7\%$ and diameters ranging from 45 to 239 μm are plotted in Figure 7a. The decrease in particle size leads to a significant acceleration of the release, where the DE factor raises from ∼5 for the 239 μm particles to ∼40 for the 45 μm particles (Figure 7b). Like for the release profiles presented in Figure 5, the data shown in Figure 7a can be very well fitted using eq 4 (see Figure S7b). A linear relation between the characteristic dissolution time τ_d and the particle size is found, where the shape parameter β decreases when τ_d increases (Figure 7c) as aforementioned in the case of variation in the drug load. All dissolution data regroup into a well-defined master curve when plotted against $(t/\tau_d)^\beta$ (Figure 7d). It is worthwhile that the dissolution time of the 45 μm particles is comparable to that of TriCor tablets, notwithstanding a drug load that is three times higher, without the help of any excipient. To the best of our knowledge, this is the fastest release reported in the literature for a fenofibrate nanocrystal formulation at such a high drug load (>70%).

CONCLUSIONS

Encapsulation of a model hydrophobic active small molecule into microgel particles was realized through a low-energy approach, capable of achieving high drug loads. We showed that cross-linkable nanoemulsions based on an alginate hydrogelator could be produced up to the concentrated regime, where minimization of surfactant quantity allowed maximizing the drug load while maintaining the ability to form stable nanoemulsions via a low-energy route. Liquidlike viscoelasticity of the nanoemulsions was observed up to ∼40 vol % in the dispersed phase, which ensures the compatibility of these nanoemulsions with their ionotropic hydrogelation into microgel particles. Uniform monodisperse particles were produced by centrifugal synthesis, followed by evaporation of

DOI: 10.1021/acs.chemmater.9b04241
Chem. Mater. 2020, 32, 498−509

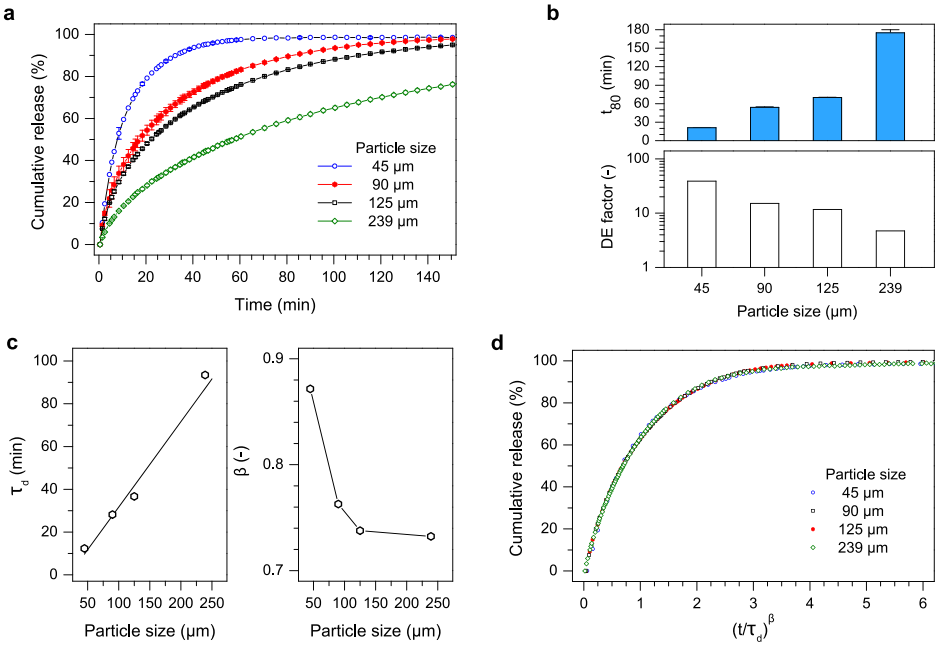

Figure 7. Influence of particle size on drug release kinetics. (a) Cumulative release profiles of 70.7% drug load dried microgel particles with size ranging from 45 to 239 μm. Data represent mean ± standard deviation. (b) Time at 80% drug release (top) and dissolution enhancement factor (bottom) as a function of particle size. (c) Fitting parameters of the Weibull equation, characteristic dissolution time τ_d (left), and shape parameter β (right), as a function of particle size. (d) Rescaled release profiles of the particles at various sizes from the data represented in (a).

both water and oil phases to induce nanocrystal formation. The drug load of the particles was tuned over a wide range (~10−70%) to investigate its influence on the structural properties and drug release performance of particles. A fully crystalline and stable form of the encapsulated API was obtained across the composition range. Calorimetric analysis and electron microscopy helped reveal the formation of nanocrystal clusters at drug loads >40%. All of our particles have shown a significant improvement in dissolution kinetics due to the considerably reduced size of the API nanocrystals compared to bulk crystals. Importantly, we have shown for the first time that the drug load plays an important role in the release kinetics of such systems, where a nonlinear evolution of the release rate with the drug load was found. This complex behavior is believed to result from the influence of nanocrystal clusters on the mass transport of the drug through the composite network. We have also demonstrated that our approach, to the best of our knowledge, yields the fastest release of stable hydrophobic nanocrystals at such high drug load. The potential for production scale-up of our low-energy method provides a way for more intensive industrial-scale throughput. In summary, this study should provide a basis for high-drug-load nanoformulations of hydrophobic compounds, especially in the outlook of advanced drug delivery applications, where achieving fast release rates at such high drug loads is often desirable.

EXPERIMENTAL SECTION

Materials. Sodium alginate (~39% in guluronic acid blocks, average molecular weight ~100 kDa), Span 80, Tween 80, fenofibrate, calcium chloride ($CaCl_2$), anisole, methanol, sodium dodecyl sulfate (SDS), ethylenediaminetetraacetic acid (EDTA) solution (0.5 M in water), and Nile red were purchased from Sigma-Aldrich and used without further purification steps.

Nanoemulsion Formation. Oil-in-water type of nanoemulsions was prepared via a low-energy approach at constant temperature (~23 °C). The continuous phase was a 2 wt % alginate-in-deionized water solution. The dispersed phase was a saturated fenofibrate-in-anisole solution. Supersaturation was obtained by adding fenofibrate in excess into anisole while stirring at 500 rpm in a closed borosilicate glass bottle overnight at room temperature. The remaining fenofibrate crystals were left to settle at the bottom of the bottle for 24 h, and the saturated solution was gently pipetted and transferred into another borosilicate glass bottle. The solubility of fenofibrate in anisole was determined by measuring the weight of 2 mL of the saturated solution before and after complete evaporation of the solvent at 50 °C overnight. A value of 0.812 ± 0.007 g mL^{-1} was found over five separate measurements.

The nanoemulsions were prepared in two steps. First, nonionic co-surfactants, namely, sorbitan monooleate (Span 80) and polysorbate (Tween 80), were mixed into the continuous phase by magnetic stirring at 700 rpm for 30 min. The surfactant blend composition was 14 wt % Span 80 and 86 wt % Tween 80, with a resulting hydrophilic−lipophilic balance (HLB) of 13.5. Spontaneous nano-emulsification was then obtained by continually dripping the dispersed phase into the continuous phase/surfactant mixture under magnetic stirring at 1000 rpm in a 20 mL glass vial. The glass vial was closed and manually shaken for a couple of seconds after the complete addition of the dispersed phase to homogenize the emulsion. Stirring was then continued for 10 min at 1000 rpm. Nanoemulsions were formed over a wide range of dispersed phase volume fraction ϕ_d with a constant surfactant/oil ratio (SOR) of 0.25, where the term oil refers to the dispersed phase. Samples with $\phi_d < 0.39$ were prepared by dilution of a concentrated nanoemulsion ($\phi_d = 0.39$) in the continuous phase.

The droplet size distribution of the nanoemulsions was determined by dynamic light scattering (DLS), using a Brookhaven NanoBrook 90Plus PALS device operating at a fixed scattering angle of 90°. The nanoemulsions were diluted to $\phi_d \sim 0.001$ in deionized water prior to measurements to prevent multiple scattering. All DLS measurements were performed at 25 °C using capped poly(methyl methacrylate) cuvettes. For each sample, the scattered intensity was collected over 1 min to determine the correlation function, and the size distribution was calculated from the correlation function by the software using a cumulant analysis. Each measurement was done in quintuplicate. The

DOI: 10.1021/acs.chemmater.9b04241
Chem. Mater. 2020, 32, 498−509

polydispersity index (PDI) was defined as $(\delta d/\bar{d})^2$, where δd and $\bar{d}$, respectively, correspond to the standard deviation and the mean of the hydrodynamic diameter distribution.

Rheological Characterization of Nanoemulsions. Shear viscoelasticity properties of nanoemulsions were characterized using a TA Instruments DHR-3 stress-controlled rotational rheometer with an upper-cone geometry (diameter = 60 mm, cone angle = 1.004°, truncated gap = 29 μm) and a lower-plate geometry equipped with a Peltier temperature control system. Deionized water was placed in the solvent trap located on top of the upper-tool cone to limit sample evaporation during the measurements. Continuous steady-state shear flow curves were recorded by carrying out shear rate sweeps from 0.1 to 300 s^{-1}. The transient shear stress was recorded for each shear rate value, and the steady-state plateau was defined as the average stress measured over 90 s with less than 5% in variation. Linear viscoelastic moduli of nanoemulsions were measured by performing small-amplitude oscillatory shear frequency sweeps, where the angular frequency ω was varied from 100 to 0.1 rad s^{-1} (each frequency sweep took ~15 min). The strain amplitude was set to a fixed value ranging from 0.1 to 1% depending on the sample to obtain a well-defined stress sine wave without exceeding the limit of linearity. All measurements were performed at 25 °C.

Particle Synthesis. Microgel particles were formed by centrifugal dripping. Briefly, a nanoemulsion precursor was pushed through a needle tip (30 gauge Nordson Optimum stainless steel tips, inner diameter = 150 μm, length = 12.7 mm) using centrifugal force; the resulting nanoemulsion drops were collected into an aqueous solution (DI water) containing 6 wt % (575 mM) calcium chloride to induce ionotropic gelation of the continuous alginate phase of the nanoemulsion. A laboratory-scale device was set up using an Eppendorf 5702 centrifuge equipped with a four swing-buckets rotor. Concentric syringe-in-centrifuge tubes were used to generate the cross-linked drops; each tube has an inner syringe containing the nanoemulsion precursor (~2.5 mL) and an outer 50 mL Falcon centrifuge tube containing the 575 mM $CaCl_2$ solution (~15 mL). The initial distance between the end of the needle tip and the free surface of the calcium chloride bath was 5 mm. Drop generation was carried out at a constant relative centrifugal force (RCF) of 110g to obtain an average particle diameter of ~350 μm. Importantly, the chosen RCF is contained within the so-called dripping without satellite regime[49] to ensure a monomodal drop size distribution. This device yields a particle throughput of ~20 mL h^{-1}. The nanoemulsion microgel particles were left in the calcium chloride bath for 1 h following the centrifugal dripping process to complete the cross-linking of the continuous phase of the nanoemulsion. The particles were then recovered from the calcium chloride bath using a qualitative filter paper (VWR, 25 μm particle retention pore size) and washed with DI water in a 100 mL glass beaker. The filtration and washing steps were repeated twice, and the particles were recovered and layered on glass Petri dishes.

Drying of the particles was then performed by placing the Petri dishes in an oven at 50 °C for 4 days to induce crystallization of the fenofibrate confined in the nanoemulsion droplets within the alginate matrix. Given the relatively large amount of particles (~4.45×10^5 particles per batch) placed on the Petri dishes, particle agglomeration occurred during the drying process due to capillary forces. Separation of the dried particles was carried out using a standard sieve (Dual Manufacturing Co., Inc.) with a 250 μm mesh opening size (slightly superior to the largest dried particle size). This sieving procedure allowed to efficiently produce large amounts of dried particles for full characterization while eliminating agglomeration issues, where the "effective" particle size (i.e., the agglomerate size) can greatly influence the release properties. Additionally, control experiments were performed to ensure that particle separation by sieving did not influence the release properties comparatively to particles that were dried far apart from each other, i.e., where no agglomeration occurred during the drying process (see details in the Supporting Information).

Smaller particles were obtained by size reduction of the primary dried particles to explore the influence of particle size on release properties. The particle size was reduced by sequentially forcing the primary dried particles through standard sieves (Dual Manufacturing Co., Inc.) with smaller mesh opening sizes, namely, 125, 90, and 45 μm (see Figure S9).

Optical Microscopy. The particle size distribution was determined using a Zeiss Axio Observer A1 inverted microscope equipped with an Andor Clara CCD digital camera. Synthesized wet microgel particles were suspended in DI water and transferred in a Nunc Lab-Tek II single-well chamber glass slide for bright-field imaging through 5× and 20× dry objectives using Andor Solis software. Image analysis was performed using ImageJ to collect statistics over 200−250 particles. Additionally, epifluorescence imaging was carried out to observe the distribution of nanoemulsion droplets within the microgel particles. For this purpose, 0.16 mM Nile red (a hydrophobic fluorescent dye, $\lambda_{ex}/\lambda_{em}$ = 550/635 nm) was co-encapsulated in fenofibrate-saturated anisole solution prior to nanoemulsion preparation. The presence of Nile red in the dispersed phase did not impact the nanoemulsion droplet size distribution or the microgel size distribution and was used only for epifluorescence imaging. A Lumen Dynamics X-Cite 120LED broad spectrum light-emitting device (LED) was used as the fluorescence source, and an Omega Optical XF101-2 long-pass filter set was used to image the fluorescent emission.

Drug Load Measurement. The drug load of the dried particles was determined by UV−vis spectroscopy. First, dried particles were ground into a fine powder using a mortar and pestle, and 30 mg of ground particles was immersed in 10 mL of methanol, followed by magnetic stirring at 700 rpm for 15 h to completely dissolve the fenofibrate nanocrystals. Methanol was selected as the solvent, given its ability to quickly dissolve fenofibrate crystals, with a solubility of ~0.059 g mL^{-1}. The solutions were then filtered through Pall Acrodisc 0.2 μm syringe filters using a 10 mL syringe to remove the alginate matrix residuals. The UV−vis absorbance spectra were recorded in a wavelength range of 150−850 nm using a Thermo Scientific NanoDrop One spectrophotometer. For every measurement, 7 μL of the sample was transferred in the microvolume cell of the spectrophotometer using a micropipette. The solvent baseline was first determined by recording the spectrum of pure methanol and subtracted from the solution spectra. A concentration−absorbance calibration curve was established using fenofibrate-in-methanol solutions with a concentration in fenofibrate ranging from 0.0001 to 0.04 g mL^{-1} (see details in the Supporting Information). The peak absorbance of fenofibrate came from its carbonyl groups and was found at a wavelength of 287 nm, which was used as the fixed wavelength for concentration−absorbance conversions. The drug load of the particles was calculated as the ratio of fenofibrate concentration to particle concentration, where the latter was always fixed at 0.003 g mL^{-1} to remain well within the linear region of the calibration curve. All measurements were done in triplicate.

Differential Scanning Calorimetry (DSC). The melting point and specific enthalpy of fusion of bulk fenofibrate and fenofibrate nanocrystals within the dried particles were determined using a TA Instruments Q2000 differential scanning calorimeter. For each measurement, 15 mg of bulk fenofibrate or the ground particle sample was placed and sealed in a Tzero aluminum pan. A temperature ramp was performed from −10 to 150 °C at a rate of 10 °C min^{-1} under an ultrapure nitrogen gas flow, using an empty sealed Tzero pan as the reference. The specific enthalpy of fusion was calculated by integration of the specific heat capacity endothermic peak area in TA Universal Analysis software, using a straight baseline between 50 and 100 °C.

X-ray Diffraction (XRD). The crystalline structure of bulk fenofibrate and fenofibrate nanocrystals within the dried particles was characterized by powder X-ray diffraction using a Philips PANalytical X'Pert Pro MPD in reflection mode ($\theta/2\theta$ goniometer setup). Ground samples were placed on a silicon crystal zero diffraction plate with a disc-shaped cavity (20 mm diameter, 0.5 mm thickness) and compressed manually using a glass slide to obtain a flat surface prior to mounting on the sample holder. The X-ray source was generated using a copper anode (Kα emission wavelength =1.54 Å), operated at an anode current of 40 mA and a high tension generator

DOI: 10.1021/acs.chemmater.9b04241
Chem. Mater. 2020, 32, 498−509

voltage of 40 kV. The diffraction angle 2θ was increased from 4 to 40° with a step size of 0.01671° at a scanning rate of 2° min^{-1}.

Transmission Electron Microscopy (TEM). The fenofibrate nanocrystals formed within the microgel particles were imaged by transmission electron microscopy. First, the nanocrystals were harvested from the dried particles. Briefly, 10 mg of ground particles was suspended in 20 mL of 0.5 M EDTA aqueous solution and magnetically stirred for 1 h. EDTA acts as a chelator on the binding Ca^{2+} of the alginate gel structure and leads to the progressive de-cross-linking of the alginate matrix, with the fenofibrate nanocrystals ending up suspended in the EDTA solution. The alginate residuals were then filtered out using Pall Acrodisc 5 μm syringe filters prior to transferring the nanocrystal suspensions into 2 mL Sorenson SafeSeal microcentrifuge tubes and centrifuging at a RCF of 14 100g for 10 min. The supernatant (EDTA solution) was pipetted out and replaced with DI water, and the nanocrystal sediment was re-suspended in DI water via vortexing for 1 min (see Figure S4). The centrifuging, supernatant replacement, and nanocrystal re-suspension steps were repeated twice to ensure complete removal of the EDTA solution. Finally, the nanocrystal suspensions were drop-cast onto formvar/carbon-coated copper 200-mesh Ted Pella TEM grids and left overnight to evaporate the DI water. Observations of the nanocrystals were carried out using an FEI Tecnai G^2 Spirit TWIN TEM equipped with a LaB_6 filament, operating at an accelerating voltage of 120 kV. Bright-field micrographs were captured using a Gatan CCD camera.

In Vitro Drug Release Experiments. The in vitro release profiles of bulk fenofibrate and fenofibrate-nanocrystal-loaded microgel particles were determined using an automated standard USP Dissolution Apparatus II (Agilent Technologies Varian VK 7025) equipped with a Cary 50 Bio UV−visible spectrophotometer and fiber optic multiplexer. The dissolution medium was prepared by dissolving 25 mM surfactant (SDS) in DI water, which raised the fenofibrate saturation solubility to ∼0.19 mg mL^{-1}.[58] For each dissolution test, the sample mass was adjusted depending on its drug load to keep the final fenofibrate concentration constant at 10% of the saturation solubility, thus ensuring sink conditions (see details in the Supporting Information). Each vessel contained 900 mL of dissolution media. All dissolution experiments were carried out at 37 °C with a paddle rotational speed of 75 rpm and were run in triplicate. Given the uncharged nature of fenofibrate, the dissolution tests were done at a constant pH of ∼6.8. The concentration of released fenofibrate in the dissolution media was tracked using UV−visible probes measuring the absorbance at a fixed wavelength of 290 nm. Blank UV−visible measurements of the dissolution media were done prior to the immersion of the samples, which were dropped manually into the vessels in less than 30 s before the automatic measurements started.

■ ASSOCIATED CONTENT

Supporting Information

The Supporting Information is available free of charge at https://pubs.acs.org/doi/10.1021/acs.chemmater.9b04241.

Calculation of internanocrystal separation in the dried microgel particles, effect of the sieving procedure on the release profile of particles, specific enthalpy of fusion and crystallinity of fenofibrate nanocrystals, fitting parameters of the Weibull function for the dissolution data, flow curves of continuous and dispersed phases of nanoemulsions, hydrodynamic diameter and PDI of nanoemulsions, fitting of the viscosity−concentration curve for the nanoemulsions, UV−vis calibration for drug load measurements, scheme of nanocrystal recovery by chelation, individual curve fitting of dissolution data, and particle size distribution for the reduced particles (PDF)

■ AUTHOR INFORMATION

Corresponding Author

*E-mail: pdoyle@mit.edu.

ORCID

Patrick S. Doyle: 0000-0003-2147-9172

Notes

The authors declare no competing financial interest.

■ ACKNOWLEDGMENTS

The authors thank Prof. Myerson for the use of the USPII dissolution apparatus. This work was supported by the Singapore National Research Foundation through an Intra-CREATE grant, Singapore A*STAR Pharma Innovation Programme Singapore, and an NSF grant CMMI-1824297.

■ REFERENCES

(1) Amidon, G. L.; Lennernäs, H.; Shah, V. P.; Crison, J. R. A Theoretical Basis for a Biopharmaceutic Drug Classification: The Correlation of in Vitro Drug Product Dissolution and in Vivo Bioavailability. *Pharm. Res.* **1995**, *12*, 413−420.

(2) Rautio, J.; Kumpulainen, H.; Heimbach, T.; Oliyai, R.; Oh, D.; Järvinen, T.; Savolainen, J. Prodrugs: design and clinical applications. *Nat. Rev. Drug Discovery* **2008**, *7*, 255.

(3) Loftsson, T.; Brewster, M. E. Pharmaceutical applications of cyclodextrins: basic science and product development. *J. Pharm. Pharmacol.* **2010**, *62*, 1607−1621.

(4) Kalepu, S.; Nekkanti, V. Insoluble drug delivery strategies: review of recent advances and business prospects. *Acta Pharm. Sin. B* **2015**, *5*, 442−453.

(5) Shegokar, R.; Müller, R. H. Nanocrystals: Industrially feasible multifunctional formulation technology for poorly soluble actives. *Int. J. Pharm.* **2010**, *399*, 129−139.

(6) Wang, G. D.; Mallet, F. P.; Ricard, F.; Heng, J. Y. Y. Pharmaceutical nanocrystals. *Curr. Opin. Chem. Eng.* **2012**, *1*, 102−107.

(7) Möschwitzer, J. P. Drug nanocrystals in the commercial pharmaceutical development process. *Int. J. Pharm.* **2013**, *453*, 142−156.

(8) Chan, H.-K.; Kwok, P. C. L. Production methods for nanodrug particles using the bottom-up approach. *Adv. Drug Delivery Rev.* **2011**, *63*, 406−416.

(9) de Waard, H.; Frijlink, H. W.; Hinrichs, W. L. J. Bottom-Up Preparation Techniques for Nanocrystals of Lipophilic Drugs. *Pharm. Res.* **2011**, *28*, 1220−1223.

(10) Zhong, J.; Shen, Z.; Yang, Y.; Chen, J. Preparation and characterization of uniform nanosized cephradine by combination of reactive precipitation and liquid anti-solvent precipitation under high gravity environment. *Int. J. Pharm.* **2005**, *301*, 286−293.

(11) Schmid, K.; Arpagaus, C.; Friess, W. Evaluation of the Nano Spray Dryer B-90 for pharmaceutical applications. *Pharm. Dev. Technol.* **2011**, *16*, 287−294.

(12) Gomez, A.; Bingham, D.; Juan, L.; Tang, K. Production of protein nanoparticles by electrospray drying. *J. Aerosol Sci.* **1998**, *29*, 561−574.

(13) Lee, A. Y.; Erdemir, D.; Myerson, A. S. Crystal Polymorphism in Chemical Process Development. *Annu. Rev. Chem. Biomol. Eng.* **2011**, *2*, 259−280.

(14) Judefeind, A.; de Villiers, M. M. Drug Loading into and In Vitro Release from Nanosized Drug Delivery Systems. In *Nanotechnology in Drug Delivery*; de Villiers, M. M.; Aramwit, P.; Kwon, G. S., Eds.; Springer: New York, NY, 2009; pp 129−162.

(15) Zuo, B.; Sun, Y.; Li, H.; Liu, X.; Zhai, Y.; Sun, J.; He, Z. Preparation and in vitro/in vivo evaluation of fenofibrate nanocrystals. *Int. J. Pharm.* **2013**, *455*, 267−275.

DOI: 10.1021/acs.chemmater.9b04241
Chem. Mater. 2020, 32, 498−509

(16) Dwyer, L. M.; Michaelis, V. K.; O'Mahony, M.; Griffin, R. G.; Myerson, A. S. Confined crystallization of fenofibrate in nanoporous silica. *CrystEngComm* **2015**, *17*, 7922−7929.
(17) Dwyer, L.; Kulkarni, S.; Ruelas, L.; Myerson, A. Two-Stage Crystallizer Design for High Loading of Poorly Water-Soluble Pharmaceuticals in Porous Silica Matrices. *Crystals* **2017**, *7*, No. 131.
(18) Mason, T. G.; Wilking, J. N.; Meleson, K.; Chang, C. B.; Graves, S. M. Nanoemulsions: formation, structure, and physical properties. *J. Phys.: Condens. Matter* **2006**, *18*, R635−R666.
(19) McClements, D. J. Nanoemulsions versus microemulsions: terminology, differences, and similarities. *Soft Matter* **2012**, *8*, 1719−1729.
(20) Gupta, A.; Eral, H. B.; Hatton, T. A.; Doyle, P. S. Nanoemulsions: formation, properties and applications. *Soft Matter* **2016**, *12*, 2826−2841.
(21) Chen, H.; Khemtong, C.; Yang, X.; Chang, X.; Gao, J. Nanonization strategies for poorly water-soluble drugs. *Drug Discovery Today* **2011**, *16*, 354−360.
(22) Badruddoza, A. Z. M.; Gupta, A.; Myerson, A. S.; Trout, B. L.; Doyle, P. S. Low Energy Nanoemulsions as Templates for the Formulation of Hydrophobic Drugs. *Adv. Ther.* **2018**, *1*, No. 1700020.
(23) McClements, D. J. Edible nanoemulsions: fabrication, properties, and functional performance. *Soft Matter* **2011**, *7*, 2297−2316.
(24) McClements, D. J.; Rao, J. Food-Grade Nanoemulsions: Formulation, Fabrication, Properties, Performance, Biological Fate, and Potential Toxicity. *Crit. Rev. Food Sci. Nutr.* **2011**, *51*, 285−330.
(25) Hashemnejad, S. M.; Badruddoza, A. Z. M.; Zarket, B.; Ricardo Castaneda, C.; Doyle, P. S. Thermoresponsive nanoemulsion-based gel synthesized through a low-energy process. *Nat. Commun.* **2019**, *10*, No. 2749.
(26) Munoz, A.; Guichard, J. P.; Reginault, P. Micronised fenofibrate. *Atherosclerosis* **1994**, *110*, S45−S48.
(27) Eral, H. B.; O'Mahony, M.; Shaw, R.; Trout, B. L.; Myerson, A. S.; Doyle, P. S. Composite Hydrogels Laden with Crystalline Active Pharmaceutical Ingredients of Controlled Size and Loading. *Chem. Mater.* **2014**, *26*, 6213−6220.
(28) van der Waarden, M. The process of spontaneous emulsification. *J. Colloid Sci.* **1952**, *7*, 140−150.
(29) Miller, C. A. Spontaneous Emulsification Produced by Diffusion—A Review. *Colloids Surf.* **1988**, *29*, 89−102.
(30) Anton, N.; Vandamme, T. F. The universality of low-energy nano-emulsification. *Int. J. Pharm.* **2009**, *377*, 142−147.
(31) López-Montilla, J. C.; Herrera-Morales, P. E.; Pandey, S.; Shah, D. O. Spontaneous Emulsification: Mechanisms, Physicochemical Aspects, Modeling, and Applications. *J. Dispersion Sci. Technol.* **2002**, *23*, 219−268.
(32) Komaiko, J. S.; McClements, D. J. Formation of Food-Grade Nanoemulsions Using Low-Energy Preparation Methods: A Review of Available Methods. *Compr. Rev. Food Sci. Food Saf.* **2016**, *15*, 331−352.
(33) Guttoff, M.; Saberi, A. H.; McClements, D. J. Formation of vitamin D nanoemulsion-based delivery systems by spontaneous emulsification: Factors affecting particle size and stability. *Food Chem.* **2015**, *171*, 117−122.
(34) Gupta, A.; Badruddoza, A. Z. M.; Doyle, P. S. A General Route for Nanoemulsion Synthesis Using Low-Energy Methods at Constant Temperature. *Langmuir* **2017**, *33*, 7118−7123.
(35) Griffin, W. C. Classification of Surface-Active Agents by "HLB". *J. Cosmet. Sci.* **1949**, *1*, 311−326.
(36) Davis, H. T. Factors determining emulsion type: Hydrophile—lipophile balance and beyond. *Colloids Surf., A* **1994**, *91*, 9−24.
(37) Meleson, K.; Graves, S.; Mason, T. G. Formation of Concentrated Nanoemulsions by Extreme Shear. *Soft Mater.* **2004**, *2*, 109−123.
(38) Ostertag, F.; Weiss, J.; McClements, D. J. Low-energy formation of edible nanoemulsions: Factors influencing droplet size produced by emulsion phase inversion. *J. Colloid Interface Sci.* **2012**, *388*, 95−102.
(39) Graves, S.; Meleson, K.; Wilking, J.; Lin, M. Y.; Mason, T. G. Structure of concentrated nanoemulsions. *J. Chem. Phys.* **2005**, *122*, No. 134703.
(40) Yang, Y.; Marshall-Breton, C.; Leser, M. E.; Sher, A. A.; McClements, D. J. Fabrication of ultrafine edible emulsions: Comparison of high-energy and low-energy homogenization methods. *Food Hydrocolloids* **2012**, *29*, 398−406.
(41) Kim, H. S.; Mason, T. G. Advances and challenges in the rheology of concentrated emulsions and nanoemulsions. *Adv. Colloid Interface Sci.* **2017**, *247*, 397−412.
(42) Quemada, D. Rheology of concentrated disperse systems and minimum energy dissipation principle. *Rheol. Acta* **1977**, *16*, 82−94.
(43) Scott, G. D. Radial Distribution of the Random Close Packing of Equal Spheres. *Nature* **1962**, *194*, 956−957.
(44) Pal, R. Modeling the Viscosity of Concentrated Nanoemulsions and Nanosuspensions. *Fluids* **2016**, *1*, No. 11.
(45) Kawada, H.; Kume, T.; Matsunaga, T.; Iwai, H.; Sano, T.; Shibayama, M. Structure and Rheology of a Self-Standing Nanoemulsion. *Langmuir* **2010**, *26*, 2430−2437.
(46) Fryd, M. M.; Mason, T. G. Advanced Nanoemulsions. *Annu. Rev. Phys. Chem.* **2012**, *63*, 493−518.
(47) Lengyel, M.; Kállai-Szabó, N.; Antal, V.; Laki, A. J.; Antal, I. Microparticles, Microspheres, and Microcapsules for Advanced Drug Delivery. *Sci. Pharm.* **2019**, *87*, 20.
(48) Ma, Y.; Björnmalm, M.; Wise, A. K.; Cortez-Jugo, C.; Revalor, E.; Ju, Y.; Feeney, O. M.; Richardson, R. T.; Hanssen, E.; Shepherd, R. K.; Porter, C. J. H.; Caruso, F. Gel-Mediated Electrospray Assembly of Silica Supraparticles for Sustained Drug Delivery. *ACS Appl. Mater. Interfaces* **2018**, *10*, 31019−31031.
(49) Eral, H. B.; Safai, E. R.; Keshavarz, B.; Kim, J. J.; Lee, J.; Doyle, P. S. Governing Principles of Alginate Microparticle Synthesis with Centrifugal Forces. *Langmuir* **2016**, *32*, 7198−7209.
(50) Di Martino, P.; Palmieri, G. F.; Martelli, S. Evidence of a metastable form of fenofibrate. *Pharmazie* **2000**, *55*, 625−626.
(51) Henry, R. F.; Zhang, G. Z.; Gao, Y.; Buckner, I. S. Fenofibrate. *Acta Crystallogr., Sect. E: Crystallogr. Commun.* **2003**, *59*, o699−o700.
(52) Heinz, A.; Gordon, K. C.; McGoverin, C. M.; Rades, T.; Strachan, C. J. Understanding the solid-state forms of fenofibrate − A spectroscopic and computational study. *Eur. J. Pharm. Biopharm.* **2009**, *71*, 100−108.
(53) Tipduangta, P.; Takieddin, K.; Fábián, L.; Belton, P.; Qi, S. A New Low Melting-Point Polymorph of Fenofibrate Prepared via Talc Induced Heterogeneous Nucleation. *Cryst. Growth Des.* **2015**, *15*, 5011−5020.
(54) Zhang, G. G. Z.; Law, D.; Schmitt, E. A.; Qiu, Y. Phase transformation considerations during process development and manufacture of solid oral dosage forms. *Adv. Drug Delivery Rev.* **2004**, *56*, 371−390.
(55) Qi, W. H.; Wang, M. P. Size effect on the cohesive energy of nanoparticle. *J. Mater. Sci. Lett.* **2002**, *21*, 1743−1745.
(56) Myerson, A. S. *Handbook of Industrial Crystallization*, 3rd ed.; Cambridge University Press: Cambridge, 2019.
(57) Godfrin, P. D.; Lee, H.; Lee, J. H.; Doyle, P. S. Photopolymerized Micelle-Laden Hydrogels Can Simultaneously Form and Encapsulate Nanocrystals to Improve Drug Substance Solubility and Expedite Drug Product Design. *Small* **2019**, *15*, No. 1803372.
(58) Jamzad, S.; Fassihi, R. Role of surfactant and pH on dissolution properties of fenofibrate and glipizide—A technical note. *AAPS PharmSciTech* **2006**, *7*, E17−E22.
(59) Grapentin, C.; Barnert, S.; Schubert, R. Monitoring the Stability of Perfluorocarbon Nanoemulsions by Cryo-TEM Image Analysis and Dynamic Light Scattering. *PLoS One* **2015**, *10*, No. e0130674.
(60) Lei, K.; Wang, X.; Li, X.; Wang, L. The innovative fabrication and applications of carvacrol nanoemulsions, carboxymethyl chitosan microgels and their composite films. *Colloids Surf., B* **2019**, *175*, 688−696.
(61) Nanda, K. K.; Sahu, S. N.; Behera, S. N. Liquid-drop model for the size-dependent melting of low-dimensional systems. *Phys. Rev. A* **2002**, *66*, No. 013208.

DOI: 10.1021/acs.chemmater.9b04241
Chem. Mater. 2020, 32, 498−509

(62) Kim, H. K.; Huh, S. H.; Park, J. W.; Jeong, J. W.; Lee, G. H. The cluster size dependence of thermal stabilities of both molybdenum and tungsten nanoclusters. *Chem. Phys. Lett.* **2002**, *354*, 165−172.
(63) Qi, W. H.; Wang, M. P. Size and shape dependent melting temperature of metallic nanoparticles. *Mater. Chem. Phys.* **2004**, *88*, 280−284.
(64) Singh, M.; Lara, S.; Tlali, S. Effects of size and shape on the specific heat, melting entropy and enthalpy of nanomaterials. *J. Taibah Univ. Sci.* **2017**, *11*, 922−929.
(65) Costa, P.; Sousa Lobo, J. M. Modeling and comparison of dissolution profiles. *Eur. J. Pharm. Sci.* **2001**, *13*, 123−133.
(66) Papadopoulou, V.; Kosmidis, K.; Vlachou, M.; Macheras, P. On the use of the Weibull function for the discernment of drug release mechanisms. *Int. J. Pharm.* **2006**, *309*, 44−50.

DOI: 10.1021/acs.chemmater.9b04241
Chem. Mater. 2020, 32, 498−509